



# Recyclable silver-decorated magnetic titania nanocomposite with enhanced visible-light photocatalytic activity



Yanyan Wang<sup>a,c</sup>, Feng Pan<sup>a,c</sup>, Wenhao Dong<sup>a,c</sup>, Leilei Xu<sup>a,c</sup>, Kai Wu<sup>c,d</sup>, Guoqing Xu<sup>a,c,e</sup>, Wei Chen<sup>a,b,c,e,\*</sup>

<sup>a</sup> Department of Chemistry, National University of Singapore, 3 Science Drive 3, 117543, Singapore, Singapore

<sup>b</sup> Department of Physics, National University of Singapore, 2 Science Drive 3, 117542, Singapore, Singapore

<sup>c</sup> Singapore-Peking University Research Center for a Sustainable Low-Carbon Future, 1CREATE Way, #15–01, CREATE Tower, Singapore 138602, Singapore, Singapore

<sup>d</sup> College of Chemistry and Molecular Engineering, Peking University, Beijing 100871, China

<sup>e</sup> National University of Singapore (Suzhou) Research Institute, 377 Lin Quan Street, Suzhou Industrial Park, Jiang Su 215123, China

## ARTICLE INFO

### Article history:

Received 23 October 2015

Received in revised form 6 January 2016

Accepted 25 February 2016

Available online 3 March 2016

### Keywords:

TiO<sub>2</sub>

Ag

Nanocomposite

Photocatalysis

Magnetic recyclability

## ABSTRACT

We report a fabrication of rationally-designed multicomponent nanocomposites comprising a magnetite core and an outer silver-decorated anatase shell and their application for visible-light photodegradation of organic compounds. The nanocomposites exhibit a well-defined core-shell structure, superparamagnetic behavior, wide-spectrum photoresponse and markedly enhanced visible-light photocatalytic activity. The enhancement of the photocatalytic activity increases with the density of decorated Ag nanoparticles in the ternary system. More importantly, the obtained nanostructured photocatalysts could be easily collected and separated by applying an external magnetic field and reused at least eight times without any appreciable reduction in photocatalytic efficiency. The enhanced photocatalytic activity and good chemical stability, in combination with the excellent magnetic recyclability, make this multifunctional nanostructure as a promising integrated system for applications in environmental remediation.

© 2016 Elsevier B.V. All rights reserved.

## 1. Introduction

There is a rapidly-growing demand for the development of materials with high efficiency, good reusability, and low cost to reduce the pollutant content in wastewater. To date, titanium dioxide (TiO<sub>2</sub>, titania) has been demonstrated to be a very suitable material in pollutants photodegradation owing to its superior photocatalytic efficiency, biological and chemical inertness, strong oxidizing ability, resistance to photocorrosion, nontoxicity, and low cost [1–6]. It is well recognized that photocatalysis is an integrated process which involves photon-irradiation induced charge carrier generation, surface/interface catalytic reaction, and post-treatment or recycling of the photocatalyst [7]. However, as a single component, titanium dioxide has low capacity to utilize solar energy (no more than 5%) due to its wide band gap and high recombination rate of photogenerated hole-electron pairs. Moreover, the separa-

tion of titanium dioxide from the treated water, especially from a large volume of water, is an expensive process.

To improve the visible-light photocatalytic activity of titanium dioxide, various strategies such as doping with nonmetal and metal [9–12], dye sensitization [13–15], and coupling with other semiconductors [16–19] have been proposed to overcome these problems. In recent years, the formation of TiO<sub>2</sub>-based composite with noble metal nanoparticle such as Au, Ag, Pt, and Pd has emerged as an effective way to improve the photocatalytic efficiency [20–22]. The decorated noble metal nanoparticles play a dual role in the photocatalytic process, including (1) the surface plasmon resonance photosensitization caused by noble metal can be utilized to harvest the visible light (accounting for 43% of solar spectrum); and (2) the formation of Schottky barrier between semiconductor and noble metal is beneficial to the separation of electron-hole pairs. Additionally, the synergistic effects induced by the components in the composite also result in an increased photostability and photocatalytic efficiency. Among all the noble metals, Ag is promising for extensive application because of its lower cost, inherent antibacterial activity, and facile preparation [23]. A number of binary Ag-TiO<sub>2</sub> composites have been designed and synthesized [24–27]. However; it is difficult to recycle these

\* Corresponding author at: Department of Chemistry, National University of Singapore, 3 Science Drive 3, 117543, Singapore.

E-mail address: [phycw@nus.edu.sg](mailto:phycw@nus.edu.sg) (W. Chen).

photocatalysts. Recycling of the photocatalyst is another important task for practical applications in aqueous environments, which allows for multiple reuses, cost reduction and additional contamination prevention.

Recently, magnetic titanium dioxide nanocomposites with core-shell structure have gained increasing attention, as they can integrate both the advantages of magnetic recovery and the superior photocatalysis performance [28]. These materials can be fast and easily removed and recycled with the help of an external magnetic field, thus preventing the loss of the catalysts during recovery and increasing the durability of the catalysts.  $\text{Fe}_3\text{O}_4$  nanoparticles are often selected in core-shell magnetic titania nanocomposites because of their unique magnetic properties and variable surface properties [29]. To immobilize  $\text{TiO}_2$  with  $\text{Fe}_3\text{O}_4$  nanoparticles, direct way and indirect way with an intermediate layer between them are often used, and high-temperature calcinations are usually applied for further formation of crystalline  $\text{TiO}_2$ . However, the magnetic characteristic of the composite catalysts will be significantly influenced by multilayer coating and high temperature calcinations, thus affecting the efficiency of recyclability [30,31]. Therefore, an approachable way to deposit crystalline  $\text{TiO}_2$  on to the magnetic nanoparticles at relatively low temperature is highly desired.

Although much effort has been devoted to optimizing the aforementioned concerns, including extension of the light absorption range, increasing charge-separation efficiency, enhancing recyclability, and integration of all these factors [32–34], it still remains a grand challenge to address these problems simultaneously and integrate distinct multiple functional components into one uniform unit at the nanoscale to maximize the photocatalytic efficiency. Herein, we report the design and fabrication of well-defined core-shell silver-decorated magnetic titania nanocomposites as a highly efficient visible-light photocatalysts with excellent magnetic recoverability, which are easy to synthesize at a relatively low temperature. The prepared nanocomposites possess multicomponent structures and multifunctional features. The morphological, structural and physical behaviors of these nanocomposites have been demonstrated and discussed. Their photocatalytic performance and reusability was evaluated using the degradation of Rhodamine B as a model system.

## 2. Experimental details

### 2.1. Materials

Iron (III) chloride hexahydrate ( $\text{FeCl}_3 \cdot 6\text{H}_2\text{O}$ ), anhydrous sodium acetate (NaAc), ethylene glycol, trisodium citrate dehydrate, silver nitrate, sodium borohydride, and titanium (IV) *n*-butoxide (TBOT,  $\text{C}_{16}\text{H}_{36}\text{O}_4\text{Ti}$ ) were purchased from Sigma-Aldrich. Rhodamine B (RhB) was purchased from Alfa Aesar. Anhydrous ethanol was purchased from International Scientific Pte Ltd. Aqueous ammonia solution (28 wt.%) was purchased from Emsure. Acetonitrile was purchased from TEDIA. Analytical grade solvents and compounds were used without further purifications for preparation. Deionized water was used for all experiments.

### 2.2. Synthesis of magnetic nanoparticles ( $\text{Fe}_3\text{O}_4$ )

The spherical magnetic particles were prepared through a solvothermal reaction. Typically, 1.35 g of  $\text{FeCl}_3 \cdot 6\text{H}_2\text{O}$ , 3.6 g of NaAc, and 0.40 g of sodium citrate were dissolved in 40 mL of ethylene glycol. The mixture were stirred vigorously for 30 min to form a homogeneous yellow solution and then transferred into a 50 mL Teflon-lined stainless-steel autoclave. The autoclave was heated at 200 °C and maintained for 16 h; then it was cooled to room tem-

perature. The product was centrifuged, washed repeatedly with ethanol and distilled water, and then dried in vacuum at 60 °C overnight.

### 2.3. Synthesis of magnetic titania nanocomposites (MTN)

The MTN was synthesized following the procedure in the literature with some modifications [35]. Briefly, 0.05 g of the as-prepared magnetite nanoparticles were well dispersed in a mixed solvent containing ethanol (75 mL), acetonitrile (25 mL), and concentrated ammonia solution (0.5 mL, 28 wt%). Then a solution of TBOT (1 mL) in ethanol (15 mL) and acetonitrile (5 mL) was added dropwise to the solution under vigorous stirring. After reaction for 1.5 h, the products were centrifuged, washed repeatedly with ethanol and acetonitrile and dried in vacuum at 60 °C overnight, denoted as  $\text{Fe}_3\text{O}_4@\text{TiO}_2$ . Next, the obtained  $\text{Fe}_3\text{O}_4@\text{TiO}_2$  nanocomposites were redispersed in a mixed solvent containing ethanol (40 mL) and deionized water (20 mL). The mixture was then transferred to a Teflon-lined stainless-steel autoclave (capacity of 100 mL). The autoclave was heated at 160 °C and maintained for 20 h. Finally, the mixture was cooled to room temperature, and the products were centrifuged, washed repeated with ethanol, and dried in vacuum at 60 °C overnight.

### 2.4. Synthesis of silver-coated magnetic titania nanocomposites (SMTN)

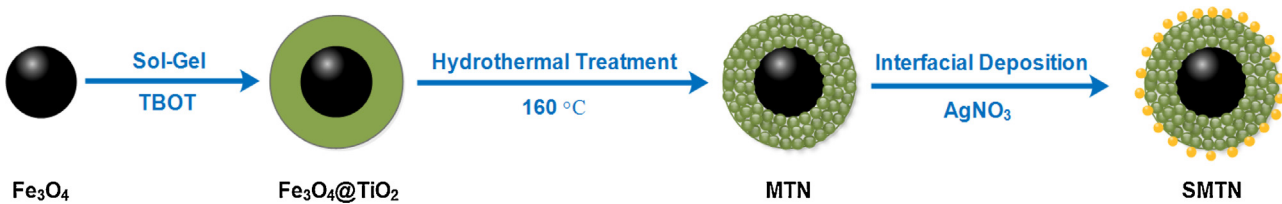
The SMTN was synthesized by using  $\text{NaBH}_4$  as the inducer. First, MTN (0.1 g) was well-dispersed into an aqueous solution (20 mL) containing  $\text{AgNO}_3$  and trisodium citrate (C/C = 1:1) and stirred vigorously for 30 min. Then a 0.01 M solution of  $\text{NaBH}_4$  (0.6 mL) was added dropwise into the above solution and mechanically stirred for 24 h. The SMTN were obtained by centrifugation (8000 r/min) for 10 min, rinsed with water twice, and dried in vacuum at 60 °C for 24 h. A series samples with different Ag loadings (0.2, 0.4, 0.8, 1, 1.2, 1.4 wt.%) were prepared, denoted as SMTN-X (X = 0.2, 0.4, 0.8, 1, 1.2, and 1.4).

### 2.5. Characterization

Transmission electron microscopy (TEM) images were taken with a JEM-2010 transmission election microscope made by Japanese JEOL Company. Powder X-ray diffraction (XRD) patterns were recorded on a Bruker on a Rigaku D/MAX 2500 diffractometer with Ni-filtered Cu K radiation (40 kV, 40 mA). Energy-dispersive X-ray spectroscopy (EDX) was used for analysis of the element distribution. The nitrogen adsorption and desorption isotherms were measured by a Nova 2200 analyzer. Before measurements, the samples were degassed in a vacuum at 150 °C for 4 h. Surface areas were calculated by the Brunauer–Emmett–Teller (BET) method, and the pore volume and pore size distributions were calculated using the Barrett–Joyner–Halenda (BJH) model. Magnetization measurements were performed on a MPM5-XL-5 superconducting quantum interference device (SQUID) magnetometer at 300 K. The content of Ag in SMTN was measured using an inductively coupled plasma (ICP) spectrometer (Perkin-Elmer). The optical properties of the samples were measured with a Shi-madzu UV-2600 UV-vis spectrophotometer. All spectroscopic measurements were performed in at least triplicate.

### 2.6. Measurement of photocatalytic activity

The photocatalytic activity was tested by examining the degradation of RhB in an aqueous solution. Ultraviolet (UV) light was illuminated by a 50W high-pressure mercury lamp. Visible light and simulated solar light were illuminated by a Xe lamp with a



**Scheme 1.** Synthetic protocol for the multicomponent nanocomposites SMTN.

UV cut-off filter ( $\lambda \geq 420 \text{ nm}$ ) and simulated solar light filter. In a typical experiment, the catalyst (10 mg) was added into 100 mL of a freshly prepared RhB solution (10 mg/L) and mechanically stirred for 10 min at room temperature to obtain a good dispersion. The system was kept in the dark for 30 min to reach saturated adsorption. Then, irradiation was started, and after a given irradiation time, 5 mL was sampled and centrifuged at 10000 rpm for the UV-vis absorbance spectrum measurement to estimate the residual RhB concentration. Each test was repeated 3 times to obtain the average results and error.

### 3. Results and discussion

#### 3.1. Synthesis and characterization of SMTN

The synthetic protocol of silver-coated magnetic titania nanocomposite is illustrated in **Scheme 1**. The magnetite particles were prepared via a solvothermal reaction based on a high temperature reduction of Fe (III) salts with ethylene glycol in the presence of trisodium citrate [36]. The magnetite particles capped with citrate groups exhibited excellent dispersion in polar solvents such as water and ethanol, which favored the subsequent coating or modification with other oxides or polymers [37]. As revealed by TEM, the obtained magnetite particles had a nearly spherical shape with rough surface and their mean diameter was about 200 nm (**Fig. 1a**). Through a subsequent sol-gel process by hydrolysis and condensation of TBOT, a uniform and compact titania layer ( $\sim 120 \text{ nm}$  in thickness) can be formed on magnetite nanoparticle, resulting in a

well-defined core-shell structure (**Fig. 1b**). Next, the as-synthesized  $\text{Fe}_3\text{O}_4@\text{TiO}_2$  microspheres were treated by a hydrothermal process at  $160^\circ\text{C}$  in a mixed ethanol/water solvent, leading to the formation of MTN. The reaction temperature in the hydrothermal process is critical for the synthesis of the desired products. When the calcination temperature is relatively high, the magnetic characteristic of the composite catalysts will significantly decrease [30,31], so we choose relatively low calcinations temperature for the formation of crystalline  $\text{TiO}_2$ . Upon hydrothermal treatment, the  $\text{TiO}_2$  shells were no longer compact (**Fig. 1c**) but comprised many very small nanocrystals (**Fig. 1c inset**).

The crystalline structure of the samples was further investigated using powder X-ray diffraction. As shown in **Fig. 2a**, all the diffraction peaks of the obtained  $\text{Fe}_3\text{O}_4$  could be readily indexed to a face-centered cubic phase magnetite (JCPDS card No. 01-075-0449), which was marked as M. Prior to the hydrothermal treatment, the XRD pattern of  $\text{Fe}_3\text{O}_4@\text{TiO}_2$  microspheres exhibited the same feature as pure  $\text{Fe}_3\text{O}_4$  (**Fig. 2b**), indicating that the coated  $\text{TiO}_2$  shell was amorphous. After hydrothermal process, several new peaks were detected for MTN, marked as A in **Fig. 2c**, which were indexed to the characteristic crystallographic planes of anatase-phase  $\text{TiO}_2$  (JCPDS card No. 01-075-2545). This result proved the occurrence of a structural transition in the  $\text{TiO}_2$  shell, from amorphous to crystalline phase, in good agreement with the TEM results. The  $\text{N}_2$  adsorption/desorption isotherm of MTN exhibited type-IV curves (**Fig. 3a**), indicating the presence of mesopores with a pore size distribution at 11.0 nm (**Fig. 3** inset). The BET surface area and total pore volume were calculated to be  $167.1 \text{ m}^2 \text{ g}^{-1}$

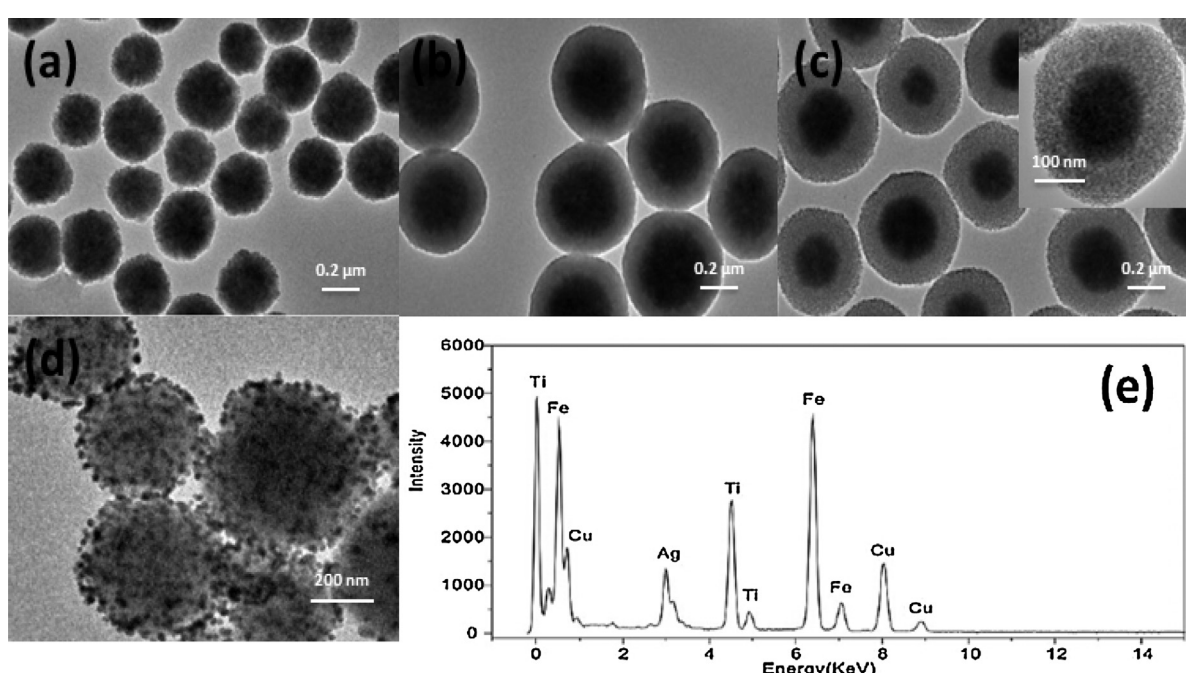


**Fig. 1.** TEM images of (a)  $\text{Fe}_3\text{O}_4$  particles, (b)  $\text{Fe}_3\text{O}_4@\text{TiO}_2$ , (c) MTN and its magnified view (inset), and SMTN (d) and the EDS spectrum of SMTN (e).

and  $0.45 \text{ cm}^3 \text{ g}^{-1}$ , respectively. We propose that the aggregation of small anatase-TiO<sub>2</sub> nanocrystals formed the non-compact shell with the existence of large number of voids between neighboring nanocrystals, thereby resulting in the formation of mesopores. Finally, Ag nanoparticles were attached on to the surface of the MTN to obtain the target nanocomposites. TEM image of the resulting SMTN clearly shows that the surface was evenly covered by Ag nanoparticles (Fig. 1d), and we can vary the concentration of Ag precursor to control the density of Ag nanoparticles decorated on the MTN. In addition to the characteristic diffraction peaks that correspond to Fe<sub>3</sub>O<sub>4</sub> and TiO<sub>2</sub>, the wide-angle XRD patterns of the SMTN show other four characteristic diffraction peaks indexed to the cubic-phase Ag (JCPDS card No. 04-0783), labeled with the symbol S (Fig. 2d). According to the Debye–Scherrer equation [38], the size of the Ag nanoparticles was estimated to be about 10 nm. The EDX characterization demonstrates that the SMTN contained three necessary and diagnostic elements of the precursors, Fe, Ti, and Ag (Fig. 1e), indicating that the obtained nanocomposites were composed of the target materials. The N<sub>2</sub> adsorption/desorption isotherm of SMTN also exhibited type-IV curves (Fig. 3b). The BET surface area of  $126.2 \text{ m}^2/\text{g}$  average pore sizes of 8.8 nm and pore volume of  $0.43 \text{ cm}^3 \text{ g}^{-1}$  for the resulting SMTN were slightly smaller than that of MTN after the deposition of the Ag nanoparticles.

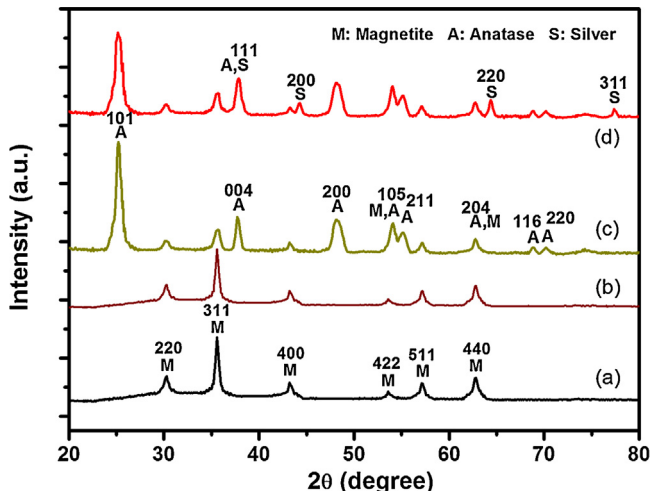


Fig. 2. The wide-angle XRD patterns of (a) Fe<sub>3</sub>O<sub>4</sub> particles, (b) Fe<sub>3</sub>O<sub>4</sub>@TiO<sub>2</sub>, (c) MTN, and (d) SMTN.

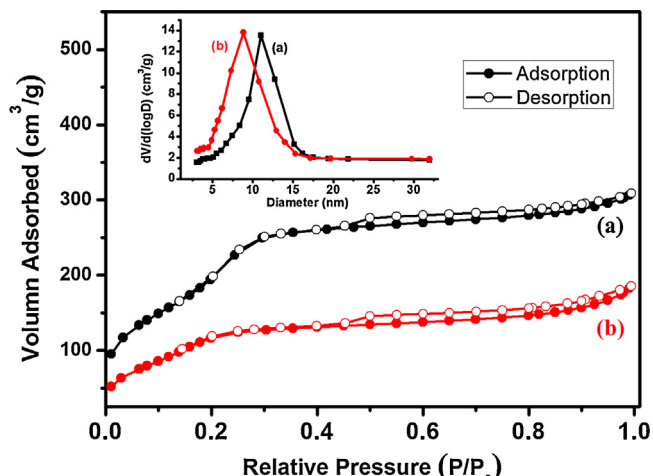


Fig. 3. The nitrogen adsorption-desorption isotherms and pore size distribution (inset) of (a) MTN and (b) SMTN.

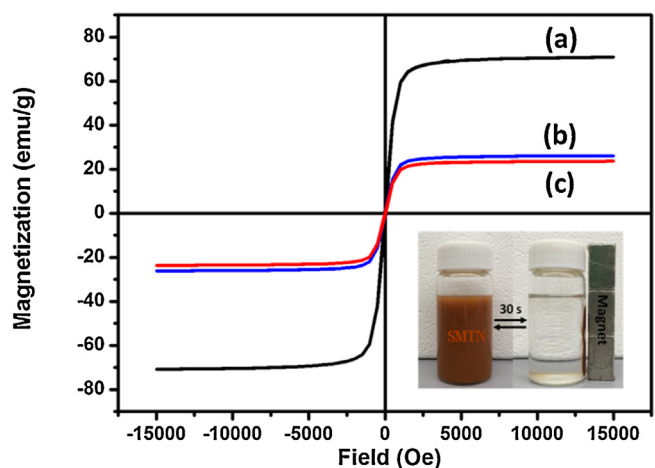


Fig. 4. The magnetic hysteresis loops of pure Fe<sub>3</sub>O<sub>4</sub> (a), MTN (b), SMTN (c), and the separation-recovery process of SMTN (inset).

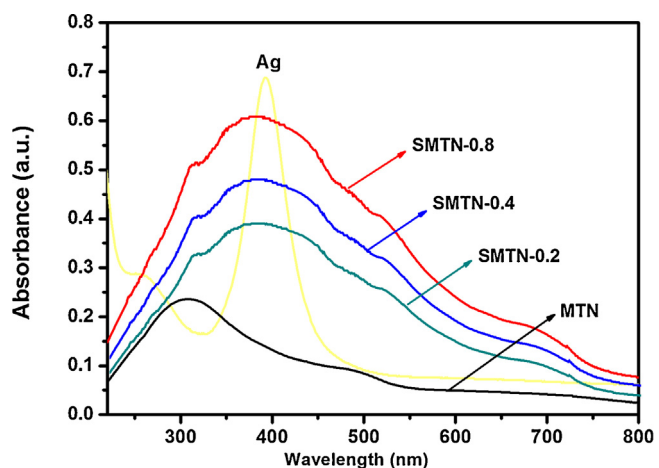
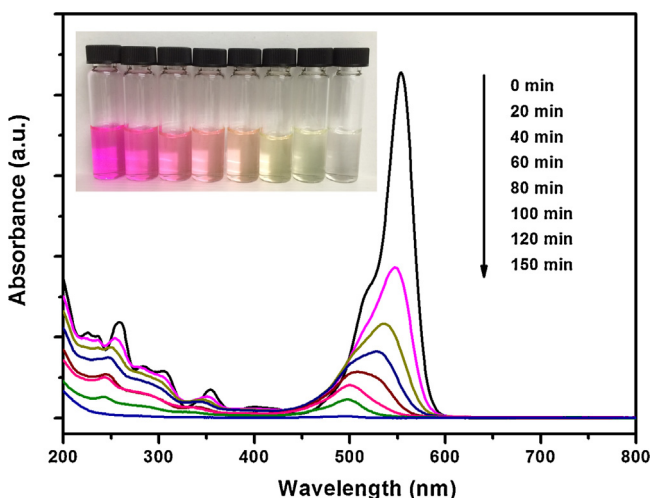


Fig. 5. The UV-vis spectra of MTN, Ag, and SMTN with different Ag loadings in aqueous solution.

The magnetic measurements on Fe<sub>3</sub>O<sub>4</sub> nanoparticles, MTN and SMTN are shown in Fig. 4. There was no obvious hysteresis for all the samples, suggesting that they all exhibit superparamagnetic behavior at room temperature. The magnetization saturation values were measured to be 70.5, 26.0 and 23.5 emu g<sup>-1</sup> for Fe<sub>3</sub>O<sub>4</sub>, MTN and SMTN, respectively. Owing to the approachable synthesis routine, after coating and calcination, SMTN still possessed relatively high magnetization saturation. Therefore, it can be quickly separated and simply recovered by applying external magnetic field (Fig. 4 inset). The technology of magnetic separation is easier to be applied than the traditional filtration and centrifugal separation and shows promising potential in large scale industrial applications [39].

### 3.2. Photocatalytic activity of SMTN

The UV-vis spectra were conducted to assess the optical property of prepared SMTN. As illustrated in Fig. 5, there was a strong absorption at wavelength shorter than 400 nm in MTN, attributing to the electronic transitions from the valence band into the conduction band (O<sub>2p</sub>-Ti<sub>3d</sub>) [40]. The MTN had little absorption between 400 and 800 nm; while in the UV-vis spectra of SMTN, a notable and broad absorption can be observed in the visible light region, arising from the SPR effect of Ag nanocysts. [41] Moreover, the absorbance intensity gradually increased with higher Ag content in the SMTN. These results indicate that after Ag



**Fig. 6.** UV-vis spectrum and photograph (inset) of the RhB solution catalyzed by SMTN under solar light for different durations.

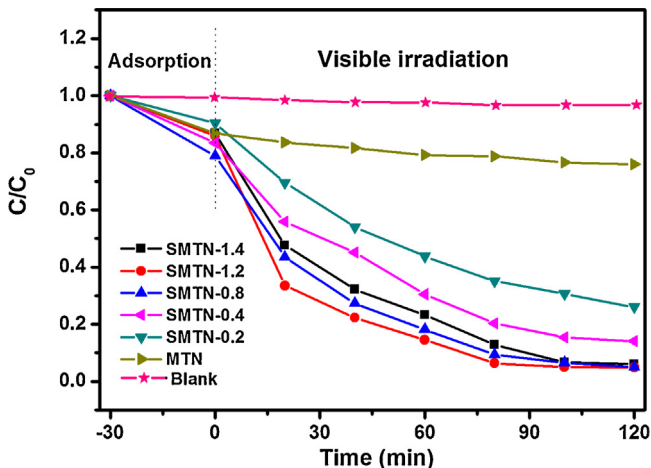


**Fig. 7.** The photocatalytic degradation curves of RhB by SMTN with different Ag loadings under visible irradiation.

nano-particles decoration the photoresponse range was extended and the photoabsorption ability was enhanced.

Photocatalytic activities of the SMTN were investigated through examining the degradation of RhB in an aqueous solution. As shown in Fig. 6, the maximum absorption of RhB decreased from 554 to 535, 522, 510, and 496 nm with the increase of the reaction time. The sharp decrease of the major absorption band indicates that SMTN exhibited excellent photocatalytic activity for the degradation of RhB. The degradation rate was very fast at the beginning of the irradiation and became slow. Meanwhile, the color of the reactive suspension changes gradually from pink to light green (Fig. 6 inset). According to the previous results reported, this hypochromic shift of the absorption band is ascribed to the formation of a series of N-deethylated intermediates in a stepwise manner, since the N-deethylation reaction of RhB is usually observed as a surface reaction induced by the active oxygen species on the catalyst and it occurs easily in the reaction systems with high specific surface area [42–44].

The effect of Ag loading on the photocatalytic activity of SMTN was also investigated. As shown in Fig. 7, the SMTN-1.2 possessed the highest photocatalytic activity among as-prepared samples. When the Ag loading lower than 1.2 wt.%, the photocatalytic activity of SMTN increased with higher Ag loading; when the Ag loading exceeded 1.2 wt.%, the photocatalytic activity of SMTN started to

**Table 1**

Comparison of adsorption and photocatalytic activity of SMTN with different silver loadings under UV, visible light and solar light. (A, adsorption and D, degradation).

Sample	UV Irradiation		Visible Irradiation		Solar Irradiation	
	A <sup>*</sup> (%)	D <sup>*</sup> (%)	A <sup>*</sup> (%)	D <sup>*</sup> (%)	A <sup>*</sup> (%)	D <sup>*</sup> (%)
MTN	21.9	95.5	13.3	26	17.6	68.6
SMTN-0.2	10	90.2	10	74	15.8	78.3
SMTN-0.4	14	91.6	16.6	86	14.5	93.2
SMTN-0.8	16	92.2	20	95	22	97.5

decline. We proposed that the excess Ag nanoparticles can serve as the recombination center of photoinduced carriers and reduce the crystallinity of TiO<sub>2</sub> [45], thereby lowering the photocatalytic performance.

To further verify the contribution of the Ag nanoparticles, the adsorption and photodegradation of RhB were evaluated for MTN and SMTN with different Ag amounts under UV, visible and simulated solar irradiation. For comparison, blank tests without photocatalysts were also performed under identical conditions. The results are presented in Fig. 8 and Table 1. It can be clearly observed that the degradation of RhB was almost negligible in the absence of catalyst under all three irradiation conditions; while RhB can be significantly degraded after the use of photocatalysts. This confirms that photolysis was not responsible for the RhB degradation in the photocatalysis experiments. Under UV irradiation, we found that Ag nanoparticles on the surface of the MTN had little effect on the increase of photocatalytic activity under UV irradiation, as shown in Fig. 8a. The photocatalytic degradation ratio of SMTN-0.8 for RhB was 92.2%, which was similar to the control sample MTN with a photocatalytic degradation ratio of 95.5%. The variable Ag loading amounts for SMTN-0.2 and SMTN-0.4 also exhibited little contribution to the photocatalytic activity. This could be attributed to unexcited Ag nanoparticles under UV irradiation, and the photocatalytic activity was mainly derived from the MTN. Under visible irradiation, as presented in Fig. 8b, the introduction of Ag nanoparticles could significantly improve the photocatalytic activity. The photodegradation ratio of SMTN-0.8 for RhB was 95%, while that of MTN was only 26%. The photocatalytic activity of MTN under visible light could be assigned to a dye-photosensitized process, since TiO<sub>2</sub> cannot directly utilize the visible light. In the photosensitization process, degradation performance strongly depends on the direct interaction between the dye molecules and the surface of TiO<sub>2</sub>. Obviously, after loading Ag nanoparticles, RhB can have less direct interaction with the surface of TiO<sub>2</sub>. However, the photocatalytic activity of SMTN was apparently much higher than that of MTN. This indicates that the well-defined heterojunction as well as the excited Ag nanoparticles on the surface played the key role during the photocatalytic process and significantly contributed to the photocatalytic efficiency improvement. In addition, the photodegradation ratio of the SMTN for RhB increased from 74% to 95% as the Ag content increased from 0.2 wt.% for SMTN-0.2 to 0.8 wt.% for SMTN-0.8. As mentioned before, when the Ag content increased, the absorbance intensity of SMTN in the visible region was enhanced due to the surface plasmon resonance, thus resulting in the increase of photocatalytic activity. Under simulated solar irradiation, the SMTN also exhibited a higher photodegradation ratio than that of MTN, and the photodegradation ratio further increased with higher Ag nanoparticles loading, as shown in Fig. 8c. Moreover, the photodegradation ratio of the SMTN for RhB under simulated solar irradiation was slightly higher than that under visible irradiation. This slight improvement may arise from the UV irradiation in the simulated solar irradiation compared to the pure visible irradiation as the UV light has enough energy to excite TiO<sub>2</sub> and induce electron migration.

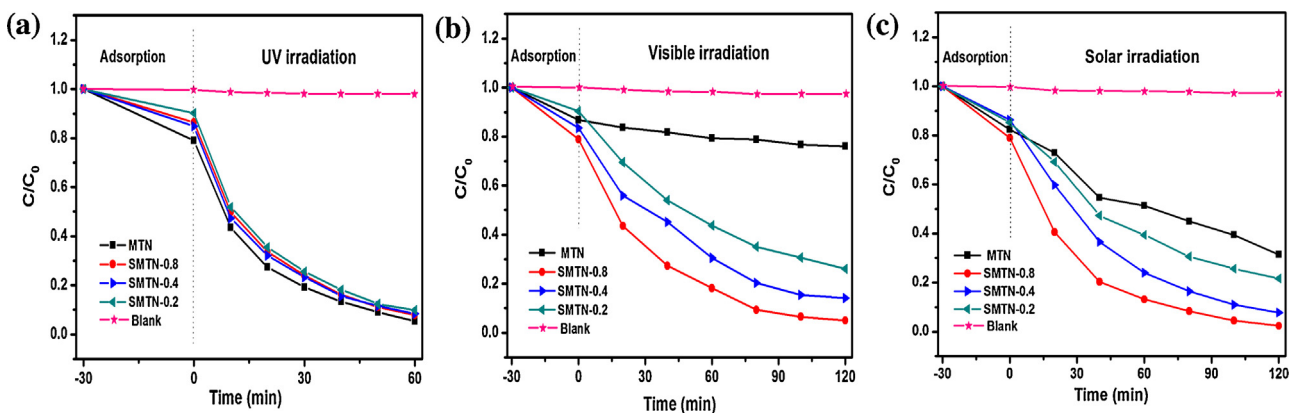
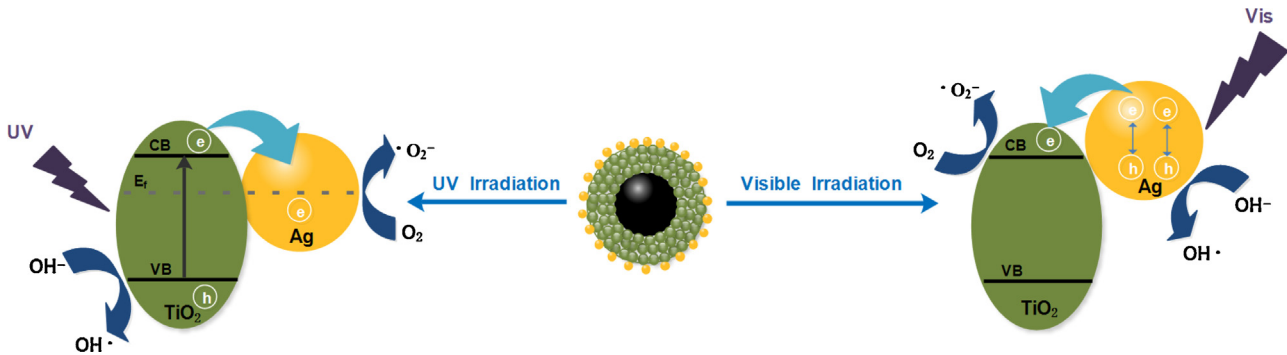


**Fig. 8.** Adsorption and photocatalytic degradation of RhB by MTN and SMTN with different silver amounts under (a) UV irradiation, (b) Visible irradiation, (c) Solar irradiation. (Blank tests: without photocatalysts).



**Scheme 2.** Schematic representation of the possible reaction mechanism of the photocatalytic procedure under different irradiation.

A schematic representation of the possible reaction mechanism of the photocatalytic procedure under different irradiation is shown in Scheme 2. Electron-migration processes are different under UV and visible-light irradiation [46–48]. Under UV irradiations, the electrons in the valence band (VB) of TiO<sub>2</sub> are excited into their corresponding conduction band (CB). The electrons in the CB of TiO<sub>2</sub> can migrate onto and then be trapped in the Ag nanoparticles due to the Schottky barrier. As a result, the holes with strong oxidizing potential can oxidize  $\text{OH}^-$  into  $\text{OH}^\cdot$  and the electrons with strong reducing potential can be transferred onto the adsorbed  $\text{O}_2$ , which can act as an electron acceptor to form superoxide radical anion,  $\cdot\text{O}_2^-$ . These active species lead to the photodegradation of RhB. Under visible-light irradiation, the electrons are transferred from the plasmon-excited Ag into the CB of TiO<sub>2</sub> and  $\text{OH}^-$  is oxidized into  $\text{OH}^\cdot$  by the holes on Ag, with the generation of  $\cdot\text{O}_2^-$  at the CB of TiO<sub>2</sub>. Similarly,  $\text{OH}^\cdot$  and  $\cdot\text{O}_2^-$  act as active species and contribute to the photodegradation of RhB.

### 3.3. Regeneration ability of SMTN

As practical recyclable catalysts, it is necessary to achieve high catalytic activity in each cycle. The recycling stability of prepared SMTN was evaluated by using SMTN-0.8 as the representative. After each photocatalytic reaction cycle, the photocatalysts were recovered by magnetic separation, washed with deionized water, and transferred into a fresh solution of RhB to undergo the reaction under identical conditions. The durability of the SMTN for the degradation of RhB under solar irradiation is shown in Fig. 9, and we can see that the photocatalytic activity was retained over several cycles, indicating the excellent reusability, which was favorable for practical applications. In addition, due to the SPR effect, as shown in Scheme 2, Ag nanocrystals may lose electron and turn to  $\text{Ag}^+$

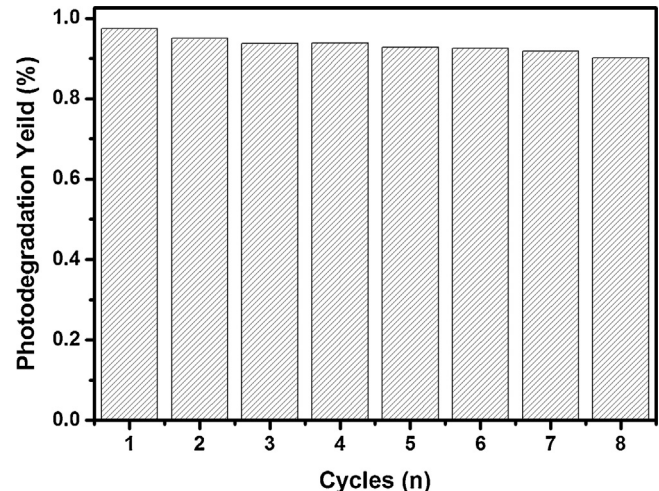


**Fig. 9.** Cycling stability of SMTN for photodegradation of RhB under solar light.

and then be released into the reaction solution. Indeed, the ICP data revealed that about 0.12 wt% Ag in the SMTN was dissolved in the solution after photocatalytic reaction for 8 h. However, the degradation ratio of RhB over SMTN-0.8 was still up to 90% after 8 consecutive cycles, as shown in Fig. 9, suggesting that the SMTN was chemically stable and mechanically robust during the photocatalytic process. Therefore, the slight conversion of Ag to  $\text{Ag}^+$  has negligible impact on the stability of SMTN.

#### 4. Conclusion

In conclusion, we demonstrate a rational design of multicomponent silver-coated magnetic titania nanocomposites with well-defined core-shell nanostructures by combining the solvothermal reaction, sol-gel process, and interfacial deposition approach. The well-designed nanocomposites exhibit significantly improved efficiency in photocatalytic degradation of RhB at room temperature even under visible light and solar light irradiation. Moreover, the obtained nanocomposites have high magnetization (23.5 emu/g), displaying convenient separability and excellent reusability without obvious loss in mass and activity. Therefore, this multifunctional nanostructure holds great promise as an efficient and recyclable photocatalyst for environmental remediation.

#### Acknowledgments

The authors acknowledge the financial support from Singapore MOE grant R143-000-542-112, Singapore National Research Foundation CREATE-SPURc program R-143-001-205-592, Academia-Industry Collaborative Innovation Foundation 20121G00421 and BY2014139 from Jiangsu Science and Technology Department and NUSRI seed fund.

#### References

- [1] A. Fujishima, T.N. Rao, D.A. Tryk, *J. Photochem. Photobiol. C: Photochem. Rev.* 1 (2000) 1–21.
- [2] X.B. Chen, S.S. Mao, *Chem. Rev.* 107 (2007) 2891–2959.
- [3] J.Y. Jing, M.H. Liu, V.L. Colvin, W.Y. Li, W.W. Yu, *J. Mol. Catal. A: Chem.* 351 (2011) 17–28.
- [4] D.Q. Zhang, G.S. Li, H.X. Li, Y.F. Lu, *Chem.—An Asian J.* 8 (2013) 26–40.
- [5] H. Park, Y. Park, W. Kim, W. Choi, *J. Photochem. Photobiol. C: Photochem. Rev.* 15 (2013) 1–20.
- [6] M. Pelaez, N.T. Nolan, S.C. Pillai, M.K. Seery, P. Falaras, A.G. Kontos, P.S.M. Dunlop, J.W.J. Hamilton, J.A. Byrne, K. O’Shea, M.H. Entezari, D.D. Dionysiou, *Appl. Catal. B: Environ.* 125 (2012) 331–349.
- [7] H. Tong, S.X. Ouyang, Y.P. Bi, N. Umezawa, M. Oshikiri, J.H. Ye, *Adv. Mater.* 24 (2012) 229–251.
- [8] F. Zuo, K. Bozhilov, R.J. Dillon, L. Wang, P. Smith, X. Zhao, C. Bardeen, P.Y. Feng, *Angew. Chem.* 124 (2012) 6327–6330.
- [9] Y. Zhang, P. Zhang, Y.N. Huo, D.Q. Zhang, G.S. Li, H.X. Li, *Appl. Catal. B: Environ.* 115–116 (2012) 236–244.
- [10] Q.J. Xiang, J.G. Yu, W.G. Wang, M. Jaroniec, *Chem. Commun.* 47 (2011) 6906–6908.
- [11] B. Liu, H.M. Chen, C. Liu, S.C. Andrews, C. Hahn, P.D. Yang, *J. Amer. Chem. Soc.* 135 (2013) 9995–9998.
- [12] S. Lei, C. Wang, D. Cheng, X. Gao, L. Chen, Y. Yan, J. Zhou, Y. Xiao, B. Cheng, *J. Phys. Chem. C* 119 (2015) 502–511.
- [13] P. Wang, J. Wang, T.S. Ming, X.F. Wang, H.G. Yu, J.G. Yu, Y.G. Wang, M. Lei, *ACS Appl. Mater. Interfaces* 5 (2013) 2924–2929.
- [14] P. Chowdhury, J. Moreira, H. Gomaa, A.K. Ray, *Ind. Eng. Chem. Res.* 51 (2012) 4523–4532.
- [15] Y.N. Huo, X.F. Chen, J. Zhang, G.F. Pan, J.P. Jia, H.X. Li, *Appl. Catal. B: Environ.* 148–149 (2014) 550–556.
- [16] G. Li, L. Wu, F. Li, P. Xu, D. Zhang, H. Li, *Nanoscale* 5 (2013) 2118–2125.
- [17] L. Wu, J. Xing, Y. Hou, F.Y. Xiao, Z. Li, H.G. Yang, *Chem.—A Eur. J.* 19 (2013) 8393–8396.
- [18] J.G. Wang, X.R. Li, X. Li, J. Zhu, H.X. Li, *Nanoscale* 5 (2013) 1876–1881.
- [19] L. Wu, F. Li, Y.Y. Xu, J.W. Zhang, D.Q. Zhang, G.S. Li, H.X. Li, *Appl. Catal. B: Environ.* 164 (2015) 217–224.
- [20] X.M. Zhang, Y.L. Chen, R.S. Liu, D.P. Tsai, *Rep. Prog. Phys.* 76 (2013) 046401.
- [21] W.B. Hou, S.B. Cronin, *Adv. Funct. Mater.* 23 (2013) 1612–1619.
- [22] Y.Z. He, P. Basnet, S.E.H. Murph, Y.P. Zhao, *ACS Appl. Mater. Interfaces* 5 (2013) 11818–11827.
- [23] D. Wang, Z.H. Zhou, H. Yang, K.B. Shen, Y. Huang, S. Shen, *J. Mater. Chem.* 22 (2012) 16306–16311.
- [24] P. Christopher, D.B. Ingram, S. Linic, *J. Phys. Chem. C* 114 (2010) 9173–9177.
- [25] Q.P. Lu, Z.D. Lu, Y.Z. Lu, L.F. Lv, Y. Ning, H.X. Yu, Y.B. Hou, Y.D. Yin, *Nano Lett.* 13 (2013) 5698–5702.
- [26] M.-V. Sofianou, N. Boukos, T. Vaimakis, C. Trapalis, *Appl. Catal. B: Environ.* 158–159 (2014) 91–95.
- [27] H.B. Yao, M.H. Fan, Y.J. Wang, G.S. Luo, W.Y. Fei, *J. Mater. Chem. A* 3 (2015) 17511–17524.
- [28] V. Polshettiwar, R. Luque, A. Fihri, H. Zhu, M. Bouhrara, J.-M. Basset, *Chem. Rev.* 111 (2011) 3036–3075.
- [29] T.A. Gad-Allah, S. Kato, S. Satokawa, T. Kojima, *Solid State Sci.* 9 (2007) 737–743.
- [30] H.R. Dong, G.M. Zeng, L. Tang, C.z. Fan, C. Zhang, X.X. He, Y. He, *Water Res.* 79 (2015) 128–146.
- [31] C.Y. Li, R. Younesi, Y.L. Cai, Y.H. Zhu, M.G. Ma, J.F. Zhu, *Appl. Catal. B: Environ.* 156–157 (2014) 314–322.
- [32] J.W. Su, Y.X. Zhang, S.C. Xu, S. Wang, H.L. Ding, S.S. Pan, G.Z. Wang, G.H. Li, H.J. Zhao, *Nanoscale* 6 (2014) 5181–5192.
- [33] D.H. baiyila, X.H. Wang, X. Li, B. sharileaodu, X.T. Li, L. Xu, Z.R. Liu, L.M. Duan, J.H. Liu, *J. Mater. Chem. A* 2 (2014) 12304–12310.
- [34] W.F. Ma, Y. Zhang, L.L. Li, L.J. You, P. Zhang, Y.T. Zhang, J.M. Li, M. Yu, J. Guo, H.J. Lu, C.C. Wang, *ACS Nano* 6 (2012) 3179–3188.
- [35] J. Liu, Z.K. Sun, Y.H. Deng, Y. Zou, C.Y. Li, X.H. Guo, L.Q. Xiong, Y. Gao, F.Y. Li, D.Y. Zhao, *Angew. Chem.* 121 (2009) 5989–5993.
- [36] Y.H. Deng, Y. Cai, Z.K. Sun, J. Liu, C. Liu, J. Wei, W. Li, C. Liu, Y. Wang, D.Y. Zhao, *J. Am. Chem. Soc.* 132 (2010) 8466–8473.
- [37] B.D. Hall, D. Zanchet, D. Ugarte, *J. Appl. Crystallogr.* 33 (2000) 1335–1341.
- [38] C.T. Yavuz, A. Prakash, J.T. Mayo, V.L. Colvin, *Chem. Eng. Sci.* 64 (2009) 2510–2521.
- [39] T. Li, W. Zhou, J.Q. Wang, Y. Qu, C.G. Tian, K. Pan, G.H. Tian, H.G. Fu, *ChemCatChem* 5 (2013) 1354–1358.
- [40] C. Liu, D. Yang, Y. Jiao, Y. Tian, Y.G. Wang, Z.Y. Jiang, *ACS Appl. Mater. Interfaces* 5 (2013) 3824–3832.
- [41] C.C. Chen, W. Zhao, J.Y. Li, J.C. Zhao, H. Hidaka, N. Serpone, *Environ. Sci. Technol.* 36 (2002) 3604–3611.
- [42] C.C. Chen, W. Zhao, P.X. Lei, J.C. Zhao, N. Serpone, *Chem.—A Eur. J.* 10 (2004) 1956–1965.
- [43] J.Y. Li, W.H. Ma, P.X. Lei, J.C. Zhao, *J. Environ. Sci.* 19 (2007) 892–896.
- [44] Q. Zhang, D.Q. Lima, I. Lee, F. Zaera, M.F. Chi, Y.D. Yin, *Angew. Chem.* 123 (2011) 7226–7230.
- [45] S. Banerjee, S.C. Pillai, P. Falaras, K.E. O’shea, J.A. Byrne, D.D. Dionysiou, *J. Phys. Chem. Lett.* 5 (2014) 2543–2554.
- [46] A. Bumajdad, M. Madkour, *Phys. Chem. Chem. Phys.* 16 (2014) 7146–7158.
- [47] S. Sarina, E.R. Waclawik, H.Y. Zhu, *Green Chem.* 15 (2013) 1814–1833.